Check for updates

Zirconium Nitride for Plasmonic Cloaking of Visible Nanowire Photodetectors

Katherine Hansen[1] · Amartya Dutta[2] · Melissa Cardona[2,3] · Chen Yang[1,2]

Abstract

Light scattered by a photodetector disturbs the probing field, resulting in noise. Cloaking is an effective method to reduce this noise. Here we investigate theoretically an emerging plasmonic material, zirconium nitride (ZrN), as a plasmonic cloak for silicon (Si) nanowire-based photodetectors and compare it with a traditional plasmonic material, gold (Au). Using Mie formalism, we have obtained the scattering cancelation across the visible spectrum. We found that ZrN cloaks produce a significant decrease in the scattering from bare Si nanowires, which is 40% greater than that obtained with Au cloaks in the wavelength region of 400–500 nm. The scattering cancelations become comparable at 550 nm, with Au providing a better scattering cancelation compared to ZrN over the wavelength region of 600–700 nm. To include the absorption and provide a measure of overall performance on noise reduction, a figure of merit (FOM), defined as the ratio of the absorption efficiency and the scattering efficiency of the cloaked nanowire to that of the bare Si nanowire, was calculated. We show that the optimized ZrN cloak provides up to 3 times enhancement of the FOM over a bare Si NW and a 60% improvement over an optimized Au-cloaked NW, in the wavelength region of 400–500 nm. An optimized Au-cloaked NW shows up to 17.69 times improvement in the wavelength region of 600–700 nm over a bare Si NW and up to a 2.7 times improvement over an optimized ZrN-cloaked NW. We also predicted the optimal dimensions for the cloaked NWs with respect to the largest FOM at various wavelengths between 400 and 650 nm.

Keywords Plasmonic cloaking · Zirconium nitride · Nanowires · Core-shell · Scattering cancelation · Emerging plasmonic materials

Introduction

Photodetectors are utilized in many applications including sensing and imaging. In the pursuit of scaling down device sizes while maintaining high responsivity, short response time, and high photoconductive gain; semiconducting nanostructures, especially nanowires, have been studied and shown

---

Katherine Hansen and Amartya Dutta contributed equally to this work.

Electronic supplementary material The online version of this article (https://doi.org/10.1007/s11468-020-01145-3) contains supplementary material, which is available to authorized users.

✉ Chen Yang
cheyang@bu.edu

[1] Department of Chemistry, Boston University, Boston, MA 02215, USA

[2] Department of Electrical and Computer Engineering, Boston University, Boston, MA 02215, USA

[3] Department of Chemistry, Purdue University, West Lafayette, IN 47907, USA

to be promising [1–3]. Semiconductor nanowires (NWs) show high light sensitivity due to the large surface area to volume ratio, as well as high photoconductive gain due to surface state promoted charge separation. Silicon is one of the most common visible light photoconductive materials due to its common use in electronics [2] and the resulting highly developed fabrication technology [4–7]. When silicon-based nanoscale photodetection devices perform in the near field of the observed object, they are disturbed by noise introduced due to light scattered by the sensor itself [2, 8, 9].

Metamaterials designed by patterning of metals, insulators, and semiconductors, such as Au/SiO2/Ag and Ag/Si, have been found recently to manipulate the scattering of nanoscale devices [10, 11]. Another effective method to reduce the field disturbance from light scattered by the photosensor itself is cloaking, where a shell is placed over the sensor which cancels the scattering due to the electromagnetic fields from the sensor, ideally over a desired range of wavelengths [8, 12, 13]. Therefore, scattering cancelation is an optimal cloaking strategy to improve the signal/noise ratio [14]. Plasmonic cloaks, which achieve scattering cancelation due to their negative

permittivity resulting in a local polarization vector antiparallel to that of the cloaked sensor, have been shown to be advantageous [14, 15]. Plasmonic cloaking is found to be particularly advantageous in the near-infrared, visible, and ultraviolet regions, where plasmonic materials possess the desired negative real permittivity values required to act as cloaks [8, 16, 17]. Another advantage of plasmonic cloaks is that they allow cloaking to occur without affecting the capacity to sense external fields [14]. Plasmonic cloaks have been shown theoretically capable of achieving scattering cancelation of spheres [17, 18] and cylinders [15]. In the solution to Maxwell's equations for both spheres [17, 19] and cylinders [15] within the quasi-static limit, where the object is smaller than the wavelength of light, the electric dipole is the dominant scattering term and can be canceled by a thin shell with a real permittivity less than the permittivity of free space. *Muhlig* et al. [20] showed that fused silica core nanoparticles with silver shells produced a noticeable suppression of the scattering. In the case of one-dimensional nanostructures, *Fan* et al. [21] showed that a gold overcoat could be engineered to suppress the light scattering of a silicon nanowire photodetector in the visible region at around 600 nm, under TM-polarized white light. It was observed that the scattering was reduced by over two orders of magnitude at the cloaking resonance. Additionally, Paniagua-Dominguez et al. demonstrated theoretically that the inverse structure, a silver metal nanowire coated with a silicon dielectric shell, also strongly reduces light scattering by three orders of magnitude compared to a bare silver wire [22]. However, designs including metals, especially Au, have challenges of incompatibility with Si fabrication. New plasmonic materials and designs more compatible with Si industrial processing are needed for greater scattering cancelation over the desired wavelength ranges and minimal interference with the absorption of the photosensor.

Transition metal nitrides recently have been identified as new plasmonic materials [23, 24]. These metal nitrides have real permittivities comparable to traditional metals such as Au, in the visible range, and unlike the traditional plasmonic metals, their plasmon properties and therefore resonance can be tuned by changing the processing methods and/or variables. Additionally, they can be fabricated with nm-level precision and can be integrated more easily into silicon-based devices without the concern of volume expansion and stress at the silicon-plasmonic material interface due to diffusion, as is common with Au which has a low eutectic temperature of 363 °C [25]. Transition metal nitrides also have exceptional mechanical properties, high melting points, and chemical stabilities, and are thus used widely as protective coatings and diffusion barriers [26]. Finally, transition metal nitrides are compatible with CMOS technology enabling lower fabrication costs, easy integration, and upscaling in mainstream industrial electronic devices, unlike gold which is a known contaminant to circuitry and thus not CMOS compatible [26, 27].

One such example of a transition metal nitride is ZrN. The optical properties of ZrN largely depend on the growth conditions and it has been shown to behave metallically when non-stoichiometric due to nitrogen deficiency [28]. Such a metallic ZrN fits a Drude-Lorentz model, resulting in dielectric functions describing metallic behavior and a cross-over wavelength, defined as the real part of the permittivity crossing zero, in the blue wavelength region of the visible spectrum [23]. Furthermore, Lalisse et al. found ZrN to have better plasmonic properties for near-field applications than gold through their figure of merit, the Faraday number, which determined ZrN nanoparticles to be 1.5 times better than Au nanoparticles, making it a better plasmonic material for the enhancement of the optical near field [29]. These properties make ZrN an ideal candidate to act as a plasmonic cloak for photosensors in the visible region.

In this work, we demonstrate theoretically, for the first time, that a conformal ZrN shell acts as a plasmonic cloak for silicon nanowire-based photosensors. We utilize a Mie formalism to gain understanding of the effectiveness of ZrN and Au cloaks on a Si NW. Key optical properties, including scattering, polarization vectors, and absorption were computed as functions of the operating wavelength of light. Dimension parameters, such as the Si nanowire diameters, shell thicknesses for ZrN and Au, were varied systematically. Optimal dimensions for each wavelength for both cloaking materials were identified. This strategy allows us to identify the effective cloak materials and dimensions for different wavelength regimes in the visible range. Specifically, based on calculations of a wide range of Si NW radii (10 nm–50 nm) and shell thicknesses (1 nm–50 nm) for both Au cloaks and ZrN cloaks, we found that a ZrN cloak on Si shows a greater scattering cancelation in 400–500 nm compared to a Au cloak, while a Au cloak gives a greater scattering cancelation than ZrN in 600–700 nm. Through calculating polarization vectors, we found that the improved scattering cancelation at a particular wavelength is due to the better matching of the polarization vectors between the core and the shell in the corresponding wavelength range. A schematic of the cloaked photodetector is shown in Fig. S2. In the cloaked Si-wire-based photodetector, the near-field scattering is reduced by the dipole polarization in the shell. We used the ratio of the absorption efficiency to the scattering efficiency as a key figure of merit to measure the overall performance of the photodetector. We found it improves for both Au- and ZrN-cloaked NWs over that of the bare Si NW. Overall, the optimal configurations in terms of material and dimensions for the highest figure of merit were identified and presented for the wavelength region of 400–700 nm. Our work demonstrates that a ZrN cloaking can be an effective approach for improving nanowire-based photosensors. Our results open the potential for designing novel-cloaked photosensors with high performance and decreased noise based on the wavelength region of interest.

Methods

The NWs are modeled as cylinders of infinite length with the incident light perpendicular to the NW axis. Using Mie formalism developed for cylinders with and without a shell, rigorous solutions to Maxwell's equations are obtained and thus the scattering efficiency and the absorption efficiency of individual layers and of the total nanowire are calculated [30–32]. The dielectric constants as a function of wavelength are obtained from previous literature [23, 33, 34]. Figure S3 summarizes the real and imaginary parts of the dielectric constants for ZrN and Au used in our study.

The scattering efficiencies were calculated for wires under unpolarized light with the nanowires being smaller than the wavelength of light in the radial direction. For sensors detecting polarized light, a similar method can be used. We consider the light to be unpolarized and break it into its transverse electric (TE) component, where the magnetic field is parallel to the nanowire axis, and its transverse magnetic (TM) component, where the electric field is parallel to the nanowire axis. In the quasi-static limit, normal incident TE and TM polarized light produce scattering due to contributions from lower order multipoles (up to dipolar contributions) [35]. We confirmed the lack of higher order multipole contributions using a case example of a 28-nm diameter Si NW with a 10-nm Au shell (Fig. S4(a)), which shows quadrupole contributions to the scattering are 3 orders of magnitude less than dipole contributions, and octupole contributions are 8 orders of magnitude less than dipole contributions. Similar features were confirmed in other dimensions. The TM modes dominate the scattering efficiency in such wires (Fig. S4(b)). We evaluate the scattering cancelation of the TE and TM components by comparing the total scattering efficiency of the cloaked nanowire to the bare nanowire, which were calculated from the Mie coefficients as follows:

$$Q_{sca}^{(TM)} = \frac{2}{k_0 r} \left\{ \sum_{n=-\infty}^{+\infty} \left(\left| a_n^{(TM)} \right|^2 + \left| b_n^{(TM)} \right|^2 \right) \right\} \quad (1)$$

$$Q_{sca}^{(TE)} = \frac{2}{k_0 r} \left\{ \sum_{n=-\infty}^{+\infty} \left(\left| a_n^{(TE)} \right|^2 + \left| b_n^{(TE)} \right|^2 \right) \right\} \quad (2)$$

The Mie coefficients a_n and b_n are calculated similarly to that described in a previous work [30], and the details are shown in the supplementary information. Here, k_0 is the wavenumber of the incident light in the medium and r is the total radius of the NW considered. The total scattering efficiency for the unpolarized light can then be calculated as the average of the scattering from the TE and TM counterparts:

$$Q_{sca} = \frac{1}{2} \left\{ Q_{sca}^{(TM)} + Q_{sca}^{(TE)} \right\} \quad (3)$$

The total scattering efficiencies were normalized by dividing the efficiencies by the highest efficiency value from the bare silicon nanowire with a diameter identical to that of the Si core in the cloaked structures.

The addition of the shell to the bare NW introduces one additional degree of freedom and can be manipulated to cancel the effect of the dominant scattering term, the dipole term. The effectiveness of this shell in canceling out the scattering term, and hence acting as a reliable cloak, can be evaluated by calculating its polarization vector antiparallel to that of the core and hence its dipole moment. The polarization is given by:

$$P = D - \varepsilon_0 E = \left(\varepsilon_j - \varepsilon_0 \right) E \quad (4)$$

Here, ε_j and ε_0 are the permittivities of the material and free space respectively, and E is the electric field calculated from Mie formalism, following a similar methodology as that described by our previous work [30]. The dipole moment p per unit length can be obtained by integrating the polarization over the entire cross-section of the cloaking shell:

$$p = \int dA \left(\varepsilon_j - \varepsilon_0 \right) E \quad (5)$$

To determine the overall efficiency of the device, we take both absorption and scattering into consideration. The absorption efficiency for the TM and TE waves were calculated by first evaluating the extinction efficiency, and then using both the scattering efficiency and the extinction efficiency as follows:

$$Q_{ext}^{(TM)} = \frac{2}{k_0 r} \left\{ \sum_{n=-\infty}^{+\infty} Re \left(b_n^{(TM)} \right) \right\} \quad (6)$$

$$Q_{abs}^{(TM)} = Q_{ext}^{(TM)} - Q_{sca}^{(TM)} \quad (7)$$

$$Q_{ext}^{(TE)} = \frac{2}{k_0 r} \left\{ \sum_{n=-\infty}^{+\infty} Re \left(a_n^{(TE)} \right) \right\} \quad (8)$$

$$Q_{abs}^{(TE)} = Q_{ext}^{(TE)} - Q_{sca}^{(TE)} \quad (9)$$

$$Q_{abs} = \frac{1}{2} \left\{ Q_{abs}^{(TE)} + Q_{abs}^{(TM)} \right\} \quad (10)$$

We further evaluated the absorption efficiency within individual layers, which is the ratio of the power absorbed over the power incident per unit length of the wire, and can thus be calculated for each layer by setting the integration limits appropriately:

$$\eta_i^{(TM)} = \frac{k_0}{2 r E_0^2} \iint Im\{\epsilon(r)\} \left| \left(E_r^{(TM)} \right)^2 + \left(E_\phi^{(TM)} \right)^2 + \left(E_z^{(TM)} \right)^2 \right| r \, dr \, d\phi$$

$$(11)$$

$$\eta_i^{(TE)} = \frac{k_0}{2 r E_0^2} \iint Im\{\epsilon 2(r)\} \left| \left(E_r^{(TE)} \right)^2 + \left(E_\phi^{(TE)} \right)^2 + \left(E_z^{(TE)} \right)^2 \right| r \, dr \, d\phi \quad (12)$$

$$\eta_i = \frac{1}{2} \left\{ \eta_i^{(TM)} + \eta_i^{(TE)} \right\} \qquad (13)$$

Here, E_0 is the magnitude of the incident field on the wire, and E_r, E_Φ, and E_z can be calculated from the Mie coefficients. Using this, we can evaluate the performance of the cloaked nanowire photosensor using the ratio of the absorption efficiency to the scattering efficiency.

We calculated the ratio of the absorption to scattering efficiency and use the ratio of that from a cloaked core-shell NW system over that of a bare Si NW as a figure of merit (FOM).

$$FOM = \frac{(\eta_i)_{c,cloaked}/(Q_{sca})_{cloaked}}{(\eta_i)_{bare}/(Q_{sca})_{bare}}$$

$$= \frac{(\eta_i)_{c,cloaked} \times (Q_{sca})_{bare}}{(\eta_i)_{bare} \times (Q_{sca})_{cloaked}} \qquad (14)$$

where $(\eta_i)_{c,\ cloaked}$ is the absorption in only the Si core and $(Q_{sca})_{cloaked}$ is the overall scattering in the cloaked system, while $(\eta_i)_{bare}$ and $(Q_{sca})_{bare}$ represent the same in a bare Si NW. For an ideal cloaked sensor, the scattering of the cloaked NW $((Q_{sca})_{cloaked})$ should correspond to a minima at the wavelength where the bare Si NW scattering is a maxima $((Q_{sca})_{bare})$. At the same time, the cloaking shell should not prevent absorption in the core, so that the absorption in the core $((\eta_i)_{c,\ cloaked})$ is sufficiently high for it to act as a photosensor.

The dimensions considered in this study are from 10 to 50 nm radii for the Si NW or the Si core in the cloaked core-shell structure, and from 1 to 50 nm for the shell thicknesses. These dimensions were chosen based on feasibility of fabrication of the different components of the cloaked system, with the radii for Si NWs chosen being the most common dimensions fabricated, and the thickness of the shell being controlled with a nm-level precision using various techniques [28, 36].

Results and Discussion

To compare the cloaking ability of a ZrN shell on a Si NW with a traditional plasmonic material such as Au, contour plots of the total scattering efficiency, as functions of the core Si NW radius and the cloaking shell thickness, were plotted in the visible wavelength region between 400 and 700 nm, at 50 nm intervals. Figure 1a and b plot such contours at two example wavelengths at 500 nm and 650 nm. Results for other wavelengths are included in the SI. The rationale of presenting 500 nm and 650 nm results here is explained below.

Figure 1a plots the scattering efficiency at 500 nm as a function of the Si core radius and the ZrN shell thickness. All scattering efficiencies were normalized to the highest scattering efficiency identified in the data set. This contour shows lower scattering efficiencies occur for small core radii and

shell thicknesses, with the lowest scattering being 0.02 at a core radius of 11 nm and a shell thickness of 11 nm. This contour provides an opportunity to systemically study the scattering at various dimensions for different cloaking materials at a given wavelength. For instance, a contour plot where Au is used as the cloaking shell at 500 nm is shown in Fig. 1c. Comparing the lowest scattering efficiencies obtained from contour plots for all wavelengths, we found that ZrN cloaks with optimized dimensions are able to perform better than Au cloaks particularly in the wavelength range of 400–500 nm. Due to this, we present the plot at 500 nm for ZrN cloaking structures here. Similarly, Au cloaks perform better in the wavelength range of 600–700 nm, so we use 650 nm as the example for Au cloaking structure.

Specifically, the contours also allow us to identify the dimensions of the cloak which provide greatest scattering cancelation to a given Si NW at a particular wavelength. A bare Si NW with a radius of 19 nm shows a maximum scattering at 500 nm compared to bare Si NWs of other dimensions (Fig. 1a and Fig. 1e black). A ZrN shell could provide further reduction of the scattering, and we identified that a ZrN shell with a 22-nm thickness shows the lowest scattering specifically for this Si core diameter (Fig. 1a). Similarly, a 25-nm thickness was identified as the most effective Au cloak for this Si core diameter (Fig. 1c). A comparison for the scattering cancelation in these two structures, the Si (19 nm radius)/ZrN (22 nm thickness) NW and the Si (19 nm radius)/Au (25 nm thickness), as a function of wavelength, is summarized and presented in Fig. 1e. Clearly, it also confirms that ZrN (Fig. 1e, green) and Au (Fig. 1e, red) cloaks with the specific thicknesses both effectively reduce the maximum scattering of the bare Si NWs at 500 nm (Fig. 1e black). In addition, this ZrN cloak also shows a consistent effective cancelation, greater than the Au cloak (Fig. 1e, red), throughout the visible wavelength region from 470 to 800 nm (Fig. 1e, green). Though the scattering efficiency values are relatively close for the ZrN cloak and the Au cloak, the better compatibility with the CMOS technology and easier integration with Si systems, as mentioned earlier, makes ZrN a superior cloaking material.

Notably, the scattering cancelation behaviors by cloaks are highly dependent on the working wavelength. This can be evident from an analysis performed for the wavelength of 650 nm. Figure 1b plots the scattering efficiency at 650 nm as a function of the Si core radius and the Au shell thickness. In Fig. 1b, the lowest value of scattering efficiency is 0.002 at a core radius of 11 nm, and a shell thickness of 6 nm. A ZrN shell, at this wavelength, however, has a scattering efficiency value of 0.004 for a core radius of 11 nm and shell thickness of 5 nm (Fig. 1d), which is greater than that of the Au cloak. To find out the dimensions for the greatest scattering cancelations, bare Si NW of radius 28 nm was identified as the dimension of a bare Si NW with the highest scattering efficiency at 650 nm. The greatest scattering cancelations for a Au
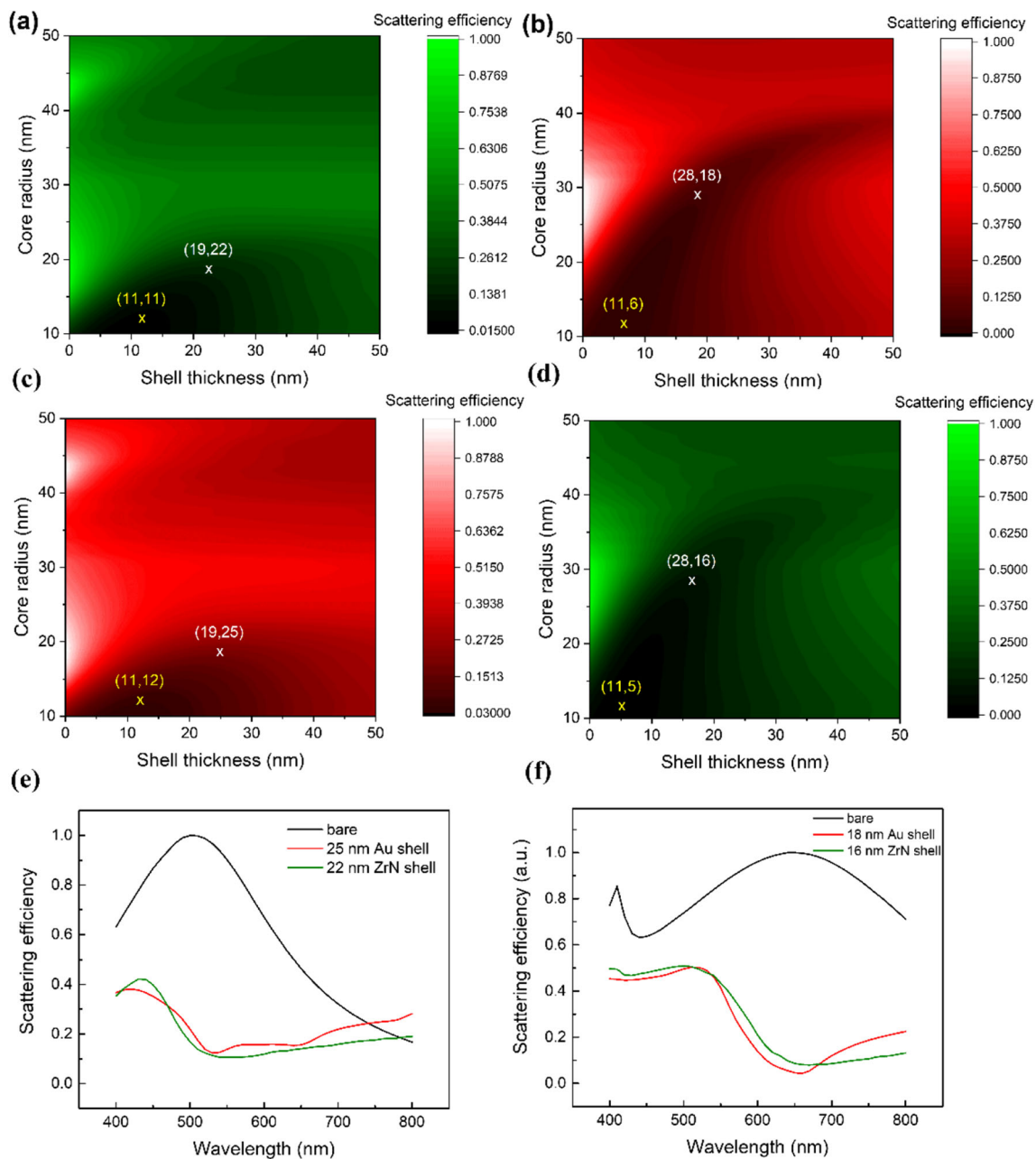
Fig. 1 Scattering efficiency under unpolarized illumination as functions of the core radius and shell thickness. **a** Contour for ZrN cloaks and **c** Au cloaks at a wavelength of 500 nm. **b** Contour for Au cloaks and **d** ZrN cloaks at a wavelength of 650 nm. Yellow and white crosses refer to the dimensions for lowest scattering efficiency and greatest scattering cancelation respectively, with the two numbers in the parentheses referring to core radius and shell thickness, in the unit of nanometer,

respectively. **e** Scattering efficiency under unpolarized illumination for a 19-nm (radius) bare Si NW (black), a 19-nm Si NW with a 25-nm Au shell (red), and a 19-nm Si NW with a 22-nm ZrN shell (green). **f** Scattering efficiency under unpolarized illumination for a 28-nm (radius) bare Si NW (black), a 28-nm Si NW with an 18-nm Au shell (red), and a 28-nm Si NW with a 16-nm ZrN shell (green)

shell and a ZrN shell for this core diameter are 0.05 (18-nm shell thickness) and 0.08 (16-nm shell thickness) respectively. At 650 nm, the Au shell provides greater scattering cancelation compared to a ZrN shell. Figure 1f plots the scattering efficiency as a function of wavelength, for these structures, i.e., the bare Si NW with a 28-nm radius, the core-shell NWs with an 18-nm Au shell (red) and a 16-nm ZrN shell (green). It can be seen that the performance of the Au-cloaked

and the ZrN-cloaked NWs are similar, up till the wavelength of 540 nm, after which the Au shell provides a greater scattering cancelation till a wavelength of 680 nm.

Figure S5a and S5b compare the contour plots at 450 nm, while Fig. S5c and S5d compare the contour plots at 600 nm. A 15-nm radius Si NW has the highest scattering efficiency for 450 nm; the greatest scattering cancelation for such a wire is with a 24-nm ZrN shell (0.16) and a 22-nm Au shell (0.24).

A 25-nm radius Si NW has the highest scattering efficiency for 600 nm, for which an 18-nm ZrN cloak (0.10) and a 16-nm Au cloak (0.06) give the greatest scattering cancelations. From our observations of the contour plots, we can thus conclude that there are two wavelength regimes: (1) between 400 and 500 nm, where a ZrN shell provides better performance in terms of scattering compared to a Au shell, and (2) between 600 and 700 nm, where a Au shell provides better performance in terms of scattering compared to a ZrN shell. In between these two wavelength regions, at 550 nm, the scattering efficiencies provided by a ZrN shell and a Au shell are similar in magnitudes.

To gain insight into what guides the differences in scattering cancelation, the polarization vector is plotted at the wavelength corresponding to greatest scattering cancelation for the optimized systems studied in Fig. 1a and c. The goal of plasmonic cloaking is to reduce the dipolar scattering, which is measured by the response of the polarization vector (P) (Eq. 4). For the core where $\varepsilon_j > \varepsilon_0$, dipolar fields are induced by the local field as a result of exciting the electric field (E). This is canceled by placing a shell which has $\varepsilon_j < \varepsilon_0$ and is ideally negative. Thus, its resulting polarization vector is antiparallel to that of the core, canceling the original dipole moment of the core itself, and thus the scattering [37]. Therefore, the greatest scattering cancelation is caused when the polarization in the

shell (P_{shell}) at any given wavelength is equal in magnitude but opposite in sign to the polarization in the core (P_{core}).

Figure 2a corresponds to the polarization vector for a 19-nm radius Si NW, while Fig. 2c corresponds to a hollow ZrN nanotube whose inner diameter is 19 nm and thickness is 22 nm, surrounded by air, at a wavelength of 500 nm. Figure 2a and c show that the polarization vectors for the Si core and the ZrN cavity are almost equal and opposite, with the maximum values of the magnitudes of the polarization vectors being within an order of difference, and the ratio of the magnitudes of the averaged polarization in the core to that in the shell being 0.7. In contrast, at the same wavelength, a hollow Au nanotube (Fig. S6a), with an inner radius of 19 nm and a thickness of 25 nm, has a maximum polarization magnitude 2.5 times larger than that of ZrN, with the corresponding ratio of P_{core} to P_{shell} being 0.5. As the dipole moment is the major contributor to the scattering, it can be concluded that the better matching between P_{core} and P_{shell} leads to greater scattering cancelation for a ZrN-cloaked NW in comparison to a Au-cloaked NW, at this wavelength.

A similar conclusion can also be stated for the better performance of Au at a wavelength of 650 nm. Figure 2b and d plot the polarization contours for a 28-nm radius Si NW, and an 18-nm hollow Au nanotube of inner radius of 28 nm surrounded by air, while Fig. S6b plots a hollow ZrN nanotube
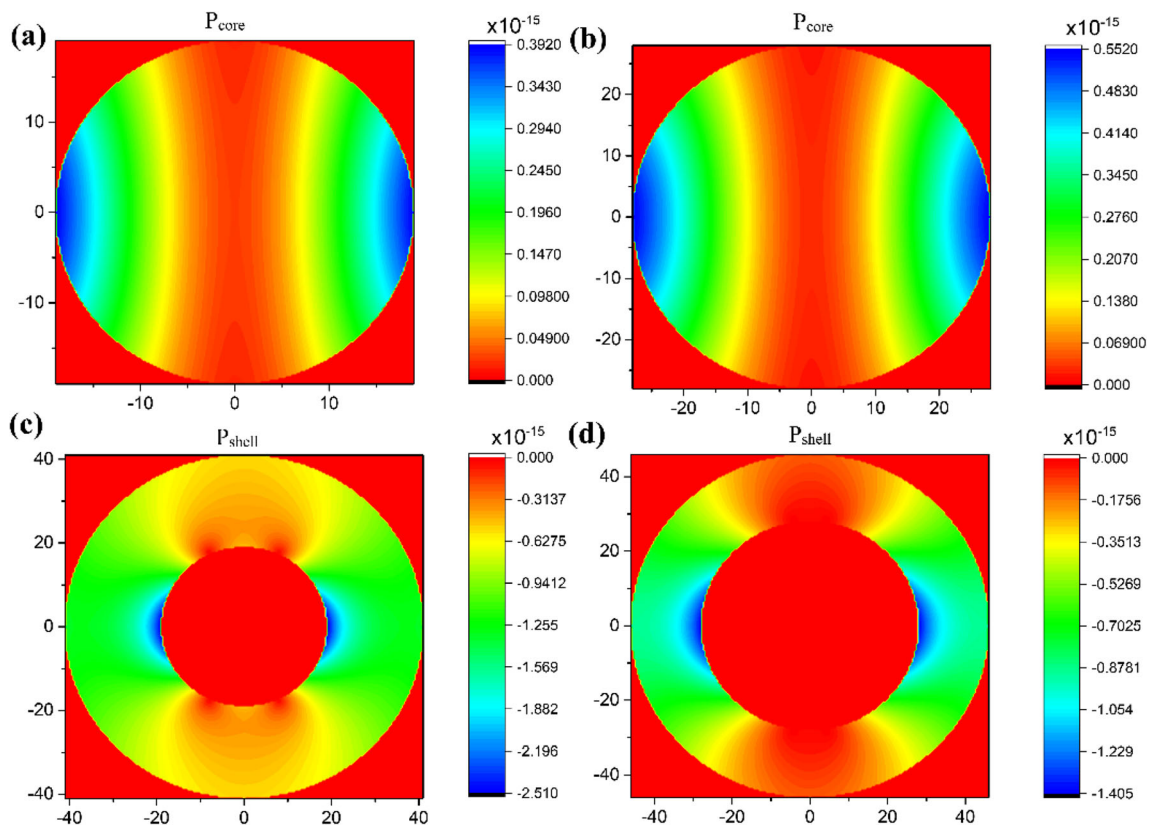

Fig. 2 a Polarization for a 19-nm Si core NW at 500 nm, b polarization for a 28-nm Si core NW at 650 nm, c polarization for a ZrN cavity with inner radius 19 nm and thickness of 22 nm at 500 nm, d polarization for a Au cavity with inner diameter 28 nm and thickness of 18 nm at 650 nm

of thickness 16 nm and inner radius of 28 nm. The maximum value of the magnitude of the polarization for the Au cavity is only two times greater than that of the Si core, with the ratio of P_{core} to P_{shell} being 0.95. The close matching of the polarization vectors leads to a very high scattering cancelation and therefore a very low scattering efficiency value of 0.05 as shown in Fig. 1b. Figure S6b, on the other hand, shows the maximum value for a 16-nm ZrN cavity being about 8% greater than that of the Au cavity, and the ratio of P_{core} to P_{shell} being 0.83. This leads to a slightly higher scattering efficiency value of 0.08. Thus, it can be concluded that the polarization of the shell being antiparallel to the polarization of the core with almost matching magnitudes plays a crucial role in scattering cancelation.

To further understand the design of Si NW-based photosensors, we analyzed the scattering efficiency for various Si NW core diameters and ZrN shell thicknesses (Fig. 3). For each core diameter, the scattering peak of the cloaked NW (green) decreases over all visible light wavelengths compared to that of the bare wire (black) as the shell thickness increases from 5 to 20 nm. As seen in the 15-nm radius Si NW case (Fig. 3a) where the bare Si NW has a scattering peak at 450 nm, two features are observed in the presence of the ZrN shell. Firstly, the scattering peak blue shifts by 20 nm, 30 nm, 40 nm, and 50 nm with shell thicknesses of 5, 10, 15, and 20 nm respectively. The blue shift is likely a consequence of increasing the total NW diameter, as previously demonstrated [38–40]. Secondly, as the ZrN shell thickness increases, the value of the scattering maxima decreases while

at the same time, the minima also start increasing. Therefore, at wavelengths below 500 nm, a 20-nm ZrN shell results in the best cloaking for this radius. However, at higher wavelengths above 600 nm, the 20-nm ZrN shell is no longer the best choice due to increase in the scattering efficiency. In this wavelength region, a 5-nm or a 10-nm ZrN shell would be more beneficial for scattering reduction for this radius of the silicon NW.

To explain the increase in the scattering at higher wavelengths for thicker ZrN shells, Fig. S7a plots the ratio of the magnitudes of the averaged polarization in the core to that in the shell as a function of wavelength for a 15-nm radius Si NW core with a 5-nm thick ZrN shell and a 20-nm thick ZrN shell. It can be seen that the Si/5 nm ZrN NW has a high ratio initially, implying that the Si core is dominating the scattering. Subsequently, the ratio starts decreasing until it is closest to 1 at 670 nm, which is where the minima of the scattering peak are. After this, the ratio goes below 1, and the ZrN shell starts controlling the scattering, due to a stronger polarization. As the 5-nm ZrN shell has a low scattering by its own (Fig. S7b), the scattering efficiency remains low in the wavelength region 670–800 nm. For the Si NW/20-nm ZrN shell, Fig. S7a shows that the ratio of P_{core} to P_{shell} crosses 1 at 480 nm, which correlates to the minima in Fig. 3a. Additionally, the polarizations are more closely matched initially, compared to the Si NW/5 nm ZrN shell, which is the reason for the smaller peak scattering efficiency values. However, the ratio drops below 1 faster than that for the 5-nm ZrN shell, and the 20-nm ZrN shell starts dominating the scattering, which combined with its

Fig. 3 Normalized scattering efficiencies under unpolarized illumination as a function of wavelength plotted for bare Si NW (black), and ZrN shell thicknesses of 5, 10, 15, and 20 nm (green) for **a** 15-nm radius silicon nanowire and core, **b** 20-nm radius silicon nanowire and core, **c** 25-nm radius silicon nanowire and core, and **d** 30-nm radius silicon nanowire and core. The legend for all labels is in **a**
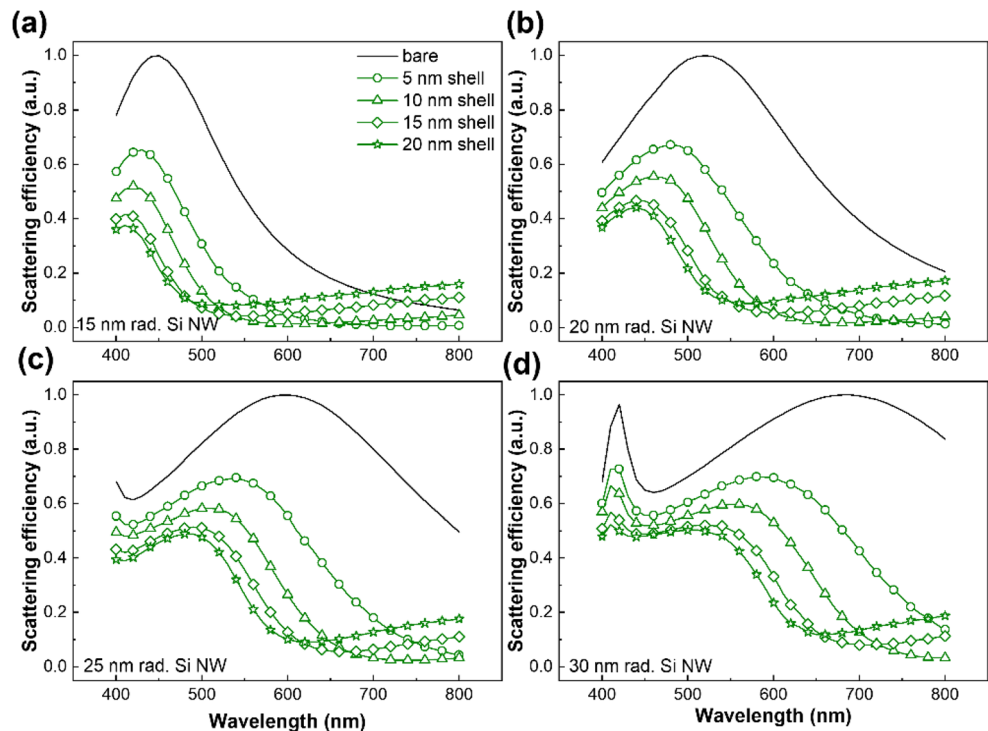
own high scattering (Fig. S7b) leads to higher values of the scattering efficiency after the minima at 480 nm. These trends of blue-shifted scattering peaks, reduced scattering with increase of the ZrN shell thickness, and increased scattering after the scattering minima are also observed over the core radius range of 20–30 nm (Fig. 3b–d). Therefore, it is important to optimize the shell thickness to get the greatest scattering cancelation at a given wavelength.

The Si NW core radius also impacts on both the photosensor performance and cloaking efficiency of the ZrN shell. The scattering spectrum of a bare Si NW is diameter dependent. The scattering peak red-shifts with increase in the Si NW diameter: 450, 520, 600, and 680 nm for Si NW radii of 15, 20, 25, and 30 nm respectively. For a given ZrN thickness, for example, 10 nm, the wavelength at which the scattering efficiency approaches zero (defined as less than scattering efficiency of 0.1) also red-shifts with the peak as the radius of the Si NW core increases. Therefore, the Si NW cores with different radii have differences in the scattering efficiencies and this is why the same ZrN shell thickness would not provide the greatest scattering cancelation for different radii of the core.

A reduction in scattering efficiency is not the only parameter to determine the performance of the photosensor; the absorbance of the incident electromagnetic radiation is also a determining factor [41]. The absorption efficiencies of a bare Si NW and a cloaked Si NW are presented in Fig. 4. Figure 4a compares the efficiencies of the optimized Si/ZrN NW (with respect to greatest scattering cancelation at 500 nm, with the core radius and shell thickness of 19 nm and 22 nm respectively), to that of the optimized Si/Au NW, with core radius and shell thickness of 19 nm and 25 nm respectively. It shows that the Si/ZrN system (solid green line) improves absorption for the whole wire over that of the bare Si NW (black line), on an average by 2.4 times at lower wavelengths (up to 550 nm) and as much as 10 times in the longer wavelength region

(650 nm–800 nm). There is a reduction in the absorption efficiency of just the Si core in the Si/ZrN system (green dashed line) on average by 40% from that of the bare NW at wavelengths up to 550 nm, with the shell contributing to the rest of the absorption. Similar features are also seen for the Si/Au system, where the Si/Au system (solid red line) improves absorption of the whole wire over that of the bare NW (solid black line) on an average by as much as 3 times at lower wavelengths (up to 520 nm), and about 2 times between 600 and 750 nm. The absorption efficiency of just the Si core in the Si/Au system (red dashed line) is comparable to that of the core in the Si/ZrN system, with the Si core in the latter absorbing slightly better in the wavelength region of 400–500 nm. We acknowledge that due to the larger value of the imaginary part of the dielectric constant of ZrN as compared to Au (Fig. S3) in the wavelength region greater than 500 nm, the loss in the ZrN shell due to the generation of evanescent waves is expected to be greater than that of Au. Notably, in the wavelength region (400–500 nm) ZrN has a lower value of the imaginary part of the dielectric constant and hence lower losses, and ZrN is found to outperform Au with respect to the FOM defined in Eq. (14) as shown later, thereby establishing that it is a superior cloak in the region of 400–500 nm.

Figure 4b shows the efficiencies of the optimized (with respect to greatest scattering cancellation at 650 nm) Si/ZrN NW, with core radius and shell thickness of 28 nm and 16 nm respectively, and compares with that of the optimized Si/Au NW, with core radius and shell thickness of 28 nm and 18 nm respectively. Similar features are observed with the cloaked systems absorbing better than the bare NW. The absorption in the core decreases, with that in the Au-cloaked system and in the ZrN-cloaked system being similar. Our results show that the absorption in the Si is decreased in the cloaked system compared to the bare Si NWs, which is not favorable. However, the observed absorption in the silicon core of the ZrN-cloaked nanowire indicates that non-negligible fields are
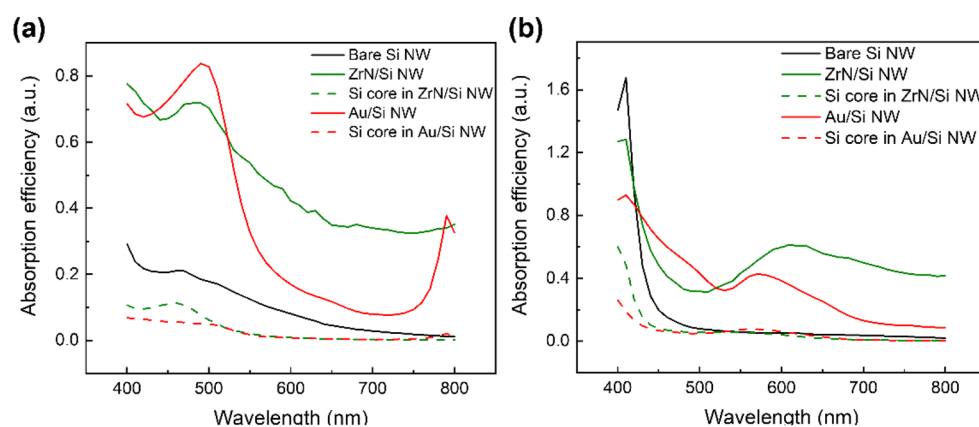

Fig. 4 Normalized absorption efficiencies under unpolarized illumination as a function of wavelength plotted for **a** 19-nm radius bare (black), 22-nm ZrN shell cloaked (solid green), and 25 nm Au shell cloaked (solid red) silicon NWs. The figure also includes the efficiencies in the core of the corresponding NWs (dashed line), **b** 28-nm radius bare (black), 16-nm ZrN shell cloaked (solid green), 18-nm Au shell cloaked (solid red) silicon NWs. The figure also includes the efficiencies in the core of the corresponding NWs (dashed line)

able to penetrate the silicon core, resulting in absorption for photocurrent generation [41]. Fan et al. experimentally observed strong absorption in a Au-cloaked Si NW and photocurrent generation similar to that of a bare nanowire [21]. Our simulation results are reasonably close to their simulated absorption data (peak absorption efficiency around 0.9 at 570 nm), showing an absorption efficiency of 0.9 at 560 nm for the 20-nm thick Au-cloaked Si NW of 50 nm diameter. This indicates the absorption in the Si core of our core-shell system could also be sufficiently high for photocurrent generation and is suitable for photosensor applications.

To evaluate the overall photosensor performance of the cloaked NWs, we calculated a FOM using the definition in Eq. (14), which calculates the enhancement in the ratio of absorption efficiency to the scattering efficiency of the cloaked NW over that of the bare Si NW. A higher FOM indicates that the probed field is less disturbed by the light scattered by the photosensor itself, and/or more absorption is achieved by the photosensor, together resulting in a better signal/noise ratio in the photosensor signal [8]. Figure 5a shows the contour plot of the FOM as functions of the core radius and the shell thickness, at 500 nm, for ZrN. The highest FOM at this wavelength was found to be 2.95, provided by an 11-nm radius Si core NW with a 9-nm thick ZrN cloak. In comparison, Fig. S8a shows the contour plot of the FOM for Au at 500 nm. The highest FOM for Au is 1.86 for an 11-nm radius Si/9 nm Au shell system, which is about 60% less than the highest FOM value for ZrN at this wavelength.

Similar dominance of a ZrN shell over a Au shell is also observed in the wavelength regime of 400–500 nm. After 550 nm, in the wavelength regime of 600–700 nm, the Au shell performs better than ZrN. Figure 5b and S8b are comparing the highest FOM for 650 nm based on the contour plots. For the Si/Au (Fig. 5b), the highest FOM value is 17.69 for a 12-nm radius Si NW with a 6-nm thick Au shell, which is 2.7 times greater than the highest FOM identified for ZrN (Fig. S8b) found in the

structure of 12-nm radius Si NW/5-nm thick ZrN shell. Therefore, when it comes to overall performance of Si NW-based photosensors in the visible regime, we notice two definite regions: (1) lower wavelength regime of 400–500 nm where ZrN cloaks will result in better performance than Au cloaks, and (2) higher wavelength regime of 600–700 nm where Au cloaks will be better compared to ZrN cloaks. Table 1 summarizes the optimal cloak material and material thickness, as well as the Si NW core radius, for the highest FOM. We notice that between 700 and 800 nm, bare Si NWs have very low scattering (between 0.05 and 0.3); therefore, the cloaking strategy by either ZrN or Au would not be effective in improving the performance. Additionally, from a fundamental point of view, we notice that the system which shows the greatest scattering cancelation in Fig. 1 does not necessarily display the highest FOM. This implies that despite having a high scattering cancelation, the absorption in these systems is not high. The FOM value of the for the cloaked ZrN system in Fig. 1 (19-nm Si core/22-nm ZrN shell) at 500-nm wavelength is 2.24, which is much lower than the value of 2.95 shown by the 11-nm core Si/9-nm ZrN shell system. Similar observations are also made at other wavelengths, as well as for the Au/Si NW systems, signifying that for best performance, both the absorption and the scattering need to be taken into consideration.

Our observations of the scattering cancelation and the FOM give us an important way of predicting the properties of a plasmonic cloak. From Fig. S3, we see that in the region between 400 and 500 nm, the real part of the dielectric constant (ε_1) for ZrN is slightly lower than that for Au, implying that in this region it is slightly more metallic. At the same time, the optical loss, indicated by the imaginary part of the dielectric constant (ε_2) for ZrN is much lower than that for Au. Thus, ZrN acts as a better plasmonic cloak in the region of 400–500 nm. Conversely, the same reason can also be argued for the better performance of Au compared to ZrN in the region of 600–700 nm.
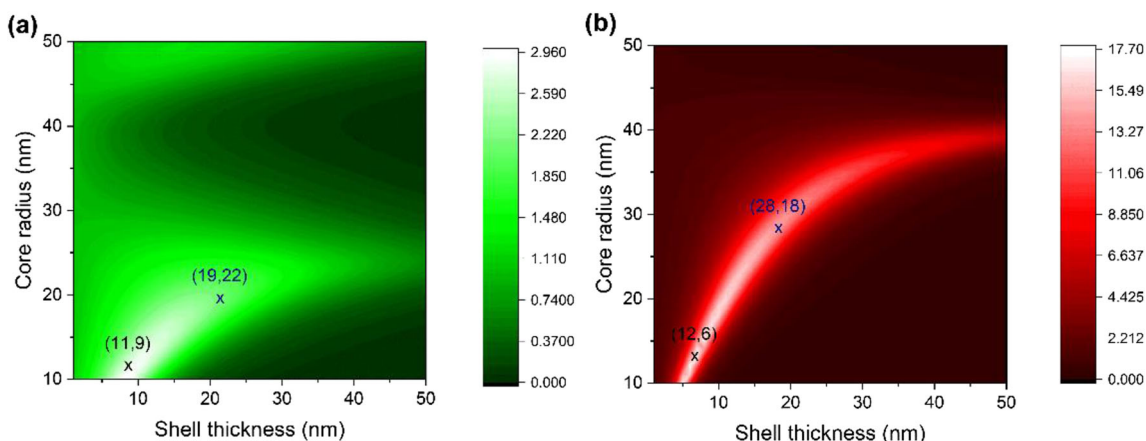

Fig. 5 FOM contour plots as functions of core radius and shell thickness for **a** a ZrN cloak at 500-nm wavelength, and **b** a Au cloak at 650-nm wavelength. Black and blue crosses refer to the dimensions for highest FOM and FOM for the optimized system in Fig. 1 with respect to scattering cancellation respectively, with the two numbers in the parentheses referring to core radius and shell thickness respectively

Table 1 Optimal cloak materials and dimensions for highest FOM values at different wavelengths. Note at 550 nm, Au was chosen here as the cloaking shell which gives the highest FOM. ZrN performs comparably with a FOM of 6.04 for a 17-nm ZrN shell

Photosensor wavelength (nm)	Si NW radius for highest scattering (nm)	Cloak material for highest FOM	Corresponding cloak thickness (nm)	Scattering efficiency	FOM
400	11	ZrN	7	0.45	1.04
450	15	ZrN	16	0.23	1.65
500	19	ZrN	18	0.17	2.38
550	22	Au	18	0.09	6.18
600	25	Au	18	0.05	10.73
650	28	Au	16	0.06	12.92

All the calculations so far were done under normal incidence of light (taken as 0° with respect to the normal). Fig. S9 shows the dependence of the scattering efficiency and the absorption efficiency on the angle of incidence for a bare 19-nm Si NW and a 19-nm Si NW with a 22-nm ZrN shell. Though the scattering by the bare NW decreases with an increase in the angle of incidence, at the same time its absorption decreases. For the ZrN-cloaked NW, the scattering is almost independent of the angle of incidence, but the total absorption, as well as the absorption in the core increases. So, it is expected that the ZrN cloak will still show an improved FOM for different angles of incidence.

Conclusion

In conclusion, ZrN has been shown to act as a plasmonic cloak, canceling the scattering of a silicon nanowire. ZrN cloaks a silicon nanowire without substantially compromising the absorption, resulting in a less-intrusive, better-performing silicon nanowire photosensor. Additionally, we have compared the performance to a traditional plasmonic material Au and have shown that ZrN cloaks fare better in terms of scattering cancelation in the wavelength region of 400–500 nm, with the performance becoming comparable at 550 nm. However, a Au cloak performs better in the regime of 600–700 nm. We also observed, through absorption-efficiency calculations, the absorption of the photosensor across the visible spectrum increases, while still maintaining high enough absorption in the silicon core to produce photocurrent, for both ZrN and Au cloaks. We used a figure of merit to incorporate both the absorption and scattering efficiencies and showed that a ZrN cloak has a higher FOM value than a Au cloak in the wavelength region of 400–500 nm, with the highest value being 2.95 at 500 nm. A Au cloak, however, performs better in the wavelength region of 600–700 nm, with the highest value

being 17.69 at 650 nm. The dimensions and materials for the plasmonic cloaks have also been included for the wavelength region of 400–650 nm. Ag can also be used as an effective cloak for a Si photosensor, and their performance is better than both Au and ZrN across the visible spectrum (Fig. S10).

Alternative plasmonic materials such as ZrN have the potential to be used as better plasmonic cloaks than traditional metals. Due to the tunability of the optical properties of these alternative materials [23, 24, 42], the magnitude of the permittivity can be controlled to best match the desired to-be cloaked core to cancel scattering. Many fabrication techniques exist for synthesis of metallic nitrides, including atomic layer deposition and molecular beam epitaxy that produce high-quality nitride films with precise thickness control, thus allowing for fabrication of sub-10-nm ZrN shells on Si NWs. Our data indicates that alternative plasmonic materials can be used to improve the measurements of near-field probing and nanoscopic imaging nanowire photosensors.

References

1. Cansizoglu H, Cansizoglu MF, Watanabe F, Karabacak T (2014) Enhanced photocurrent and dynamic response in vertically aligned In(2)S(3)/Ag core/shell nanorod array photoconductive devices. ACS Appl Mater Interfaces 6(11):8673–8682

2. Vj L et al (2011) A perspective on nanowire photodetectors: current status, future challenges, and opportunities. IEEE J Sel Top Quant Electron 17(4):1002–1032

3. Soci C, Zhang A, Bao XY, Kim H, Lo Y, Wang D (2010) Nanowire Photodetectors. J Nanosci Nanotechnol 10(3):1430–1449

4. Guo Z, Zhao DX, Liu, YC, Shen DZ, Zhang JY, Li BH (2008) Visible and ultraviolet light alternative photodetector based on ZnO nanowire/n-Si heterojunction. Appl Phys Lett 93(16):163501

5. Park H, Crozier KB (2015) Vertically stacked photodetector devices containing silicon nanowires with engineered absorption spectra. ACS Photonics 2(4):544–549

6. Meng JJ, Cadusch JJ, and Crozier KB 2019 Vertically stacked silicon nanowire photodetectors for spectral reconstruction. Conference on Lasers and Electro-Optics (Cleo), 2019

7. Um HD, Solanki A, Jayaraman A, Gordon RG, Habbal F (2019) Electrostatically doped silicon nanowire arrays for multispectral photodetectors. ACS Nano 13(10):11717–11725

8. Alu A, Engheta N (2009) Cloaking a sensor. Phys Rev Lett 102(23):233901

9. Zou Y, Steinvurzel P, Yang T, Crozier KB (2009) Surface plasmon resonances of optical antenna atomic force microscope tips. Appl Phys Lett 94(17):171107

10. Baqir MA, Choudhury PK (2017) Hyperbolic metamaterial-based UV absorber. IEEE Photon Technol Lett 29(18):1548–1551

11. Baqir MA, Farmani A, Fatima T, Raza MR, Shaukat SF, Mir A (2018) Nanoscale, tunable, and highly sensitive biosensor utilizing hyperbolic metamaterials in the near-infrared range. Appl Opt 57(31):9447–9454

12. Fleury R and Alù A 2014 Cloaking and invisibility - a review, in Forum for Electromagnetic Research Methods and Application Technologies (FERMAT)

13. Soric JC et al (2014) Controlling scattering and absorption with metamaterial covers. IEEE Trans Antennas Propag 62(8):4220–4229

14. Alu A, Engheta N (2005) Achieving transparency with plasmonic and metamaterial coatings. Phys Rev E 72:016623

15. Alu A, Rainwater D, Kerkhoff A (2010) Plasmonic cloaking of cylinders: finite length, oblique illumination and cross-polarization coupling. New J Phys 12:103028

16. Chen PY, Soric J, Alu A (2012) Invisibility and cloaking based on scattering cancellation. Adv Mater 24(44):OP281–OP304

17. Alù A, Engheta N (2007) Plasmonic materials in transparency and cloaking problems-mechanism, robustness, and physical insights. Opt Express 15(6):3318–3332

18. Monticone F, Argyropoulos C, Alu A (2012) Layered plasmonic cloaks to tailor the optical scattering at the nanoscale. Sci Rep 2:912

19. Ali A, Naqvi QA, Baqir MA (2019) Investigation of the plasmon resonance of core-shell nanoparticle in the near-infrared region. J Electromagn Waves Appl 33(18):2462–2475

20. Muhlig S et al (2013) A self-assembled three-dimensional cloak in the visible. Sci Rep 3:2328

21. Fan P et al (2012) An invisible metal–semiconductor photodetector. Nat Photonics 6(6):380–385

22. Paniagua-Dominguez R et al (2013) Broadband telecom transparency of semiconductor-coated metal nanowires: more transparent than glass. Opt Express 21(19):22076–22089

23. Naik GV, Kim J, Boltasseva A (2011) Oxides and nitrides as alternative plasmonic materials in the optical range [invited]. Opt Mater Express 1(6):1090–1099

24. Zgrabik CM, Hu EL (2015) Optimization of sputtered titanium nitride as a tunable metal for plasmonic applications. Opt Mater Express 5(12):2786–2797

25. Bal JK, Hazra S (2007) Interfacial role in room-temperature diffusion of Au into Si substrates. Phys Rev B 75(20):205411

26. Patsalas P et al (2018) Conductive nitrides: growth principles, optical and electronic properties, and their perspectives in photonics and plasmonics. Mater Sci Eng R Rep 123:1–55

27. Lefebvre A et al (2016) CMOS compatible metal-insulator-metal plasmonic perfect absorbers. Opt Mater Express 6(7):2389–2396

28. Muneshwar T, Cadien K (2015) Low temperature plasma enhanced atomic layer deposition of conducting zirconium nitride films using tetrakis (dimethylamido) zirconium and forming gas (5% H-2+95% N-2) plasma. J Vac Sci Technol A 33(3):031502

29. Lalisse A et al (2015) Quantifying the efficiency of plasmonic materials for near-field enhancement and photothermal conversion. J Phys Chem C 119(45):25518–25528

30. Ramadurgam S, Lin TG, Yang C (2014) Aluminum plasmonics for enhanced visible light absorption and high efficiency water splitting in core-multishell nanowire photoelectrodes with ultrathin hematite shells. Nano Lett 14(8):4517–4522

31. Frezza F, Mangini F, Tedeschi N (2018) Introduction to electromagnetic scattering: tutorial. J Opt Soc Am A Opt Image Sci Vis 35(1):163–173

32. Lawrence N, Dal Negro L (2010) Light scattering, field localization and local density of states in co-axial plasmonic nanowires. Opt Express 18(15):16120–16132

33. Johnson PB, Christy RW (1972) Optical constants of noble metals. Phys Rev B 6(12):4370–4379

34. Aspnes DE, Studna AA (1983) Dielectric functions and optical-parameters of Si, Ge, Gap, Gaas, Gasb, Inp, Inas, and Insb from 1.5 to 6.0 Ev. Phys Rev B 27(2):985–1009

35. Wiecha PR et al (2017) Strongly directional scattering from dielectric nanowires. ACS Photonics 4(8):2036–2046

36. Golshani N, Mohammadi V, Schellevis H, Beenakker CIM, Ishihara R (2014) Research update: reactively sputtered nanometer-thin ZrN film as a diffusion barrier between Al and boron layers for radiation detector applications. Apl Mater 2(10):100702

37. Fleury R and Alù A Cloaking and invisibility - a review, in Forum for Electromagnetic Research Methods and Application Technologies (FERMAT)

38. Ghosh PK, Debu DT, French DA, Herzog JB (2017) Calculated thickness dependent plasmonic properties of gold nanobars in the visible to near-infrared light regime. PLoS One 12(5):e0177463

39. Massa E, Maier SA, Giannini V (2013) An analytical approach to light scattering from small cubic and rectangular cuboidal nanoantennas. New J Phys 15:063013

40. Zhu J (2007) Theoretical study of the light scattering from gold nanotubes: effects of wall thickness. Mater Sci Eng A 454:685–689

41. Fleury R, Soric J, Alu A (2014) Physical bounds on absorption and scattering for cloaked sensors. Phys Rev B 89:045122

42. Ponon NK et al (2015) Effect of deposition conditions and post deposition anneal on reactively sputtered titanium nitride thin films. Thin Solid Films 578:31–37